Operating Characteristics of a Flameless Combustor Obtained By Experiments Informed Modelling

Sampat, Rishikesh; Goselink, Niek; Schrijer, Ferry; Rao, Arvind Gangoli

DOI
10.1115/GT2022-81808

Publication date
2022

Document Version
Final published version

Published in
Combustion, Fuels, and Emissions

Proceedings of ASME Turbo Expo 2022
Turbomachinery Technical Conference and Exposition
GT2022
June 13-17, 2022, Rotterdam, The Netherlands

GT2022-81808

OPERATING CHARACTERISTICS OF A FLAMELESS COMBUSTOR OBTAINED BY EXPERIMENTS INFORMED MODELLING

Rishikesh Sampat[1†], **Niek Goselink**[1], **Ferry Schrijer**[1], **Arvind Gangoli Rao**[1]
[1]Faculty of Aerospace Engineering, TU Delft, The Netherlands

ABSTRACT

Flameless Combustion is an interesting low NO_x combustion technology for gas turbine engines. In order to design systems for stringent performance standards, it is important to understand emission formation in this regime. To this end, the characteristics of a combustor capable of operating in the Flameless regime are studied. Particle Image Velocimetry and thermocouple measurements were performed to obtain the velocity field and gas temperatures respectively, in the combustor under reacting conditions. Results from experiments were used to generate an "informed" chemical reactor network (CRN) model from which, temperature and species distributions were obtained. As such, this paper presents measured data and a methodology to combine it with CRN modelling to obtain gas composition and temperature. The temperature, NO_x, CO and O_2 mole fractions obtained at three different operating conditions shall be validated with gas composition measurements in the future.

1 Introduction

Flameless Combustion (FC) is a regime of combustion that has potential for low NO_x emissions. This is of interest for gas turbine applications where low NO_x is now one of the driver parameters of combustion system design. Flameless combustion occurs in environments with highly diluted oxidiser and temperatures above the auto-ignition temperature [1] [2]. In a non-premixed system, this means that the dilution of the oxidiser stream slows the reaction enough to allow for better mixing of the oxygen and fuel resulting in a more distributed, low temperature combustion [3]. Lower peak temperatures are associated with lower thermal NO_x formation. A comprehensive overview of Flameless Combustion and its potential towards gas turbines is given in Ref [4]. The authors highlight the general understanding of FC obtained through theoretical definitions, experiments and simulations by various researchers in the community. They further mention developments aimed at transforming fundamental knowledge to more applied combustors for gas turbines.

In our case, we have a partially premixed burner modified from a FLOX burner, operating in Flameless conditions. The burner head was used on a previous combustion setup [5] with a pressurised combustion chamber having limited optical access. Temperature and gas composition measurements were done to map the operation of the combustor with natural gas as fuel. However, the flow field was not visualised through experiments and the understanding of it was limited to CFD simulations which was shown to have limitations in producing realistic estimates of temperature and hence velocities in reacting conditions. A similar combustor configuration, operating on natural gas, was tested and researched by DLR [6]. The combustor was operated at high pressures and NO_x and CO measurements were recorded. OH* chemiluminescence and planar laser induced fluorescence (PLIF) of OH were used to analyse the reaction zone. In Ref [7], the authors go on to analyze pollutant formation by CFD simulations based on a partially stirred reactor model to include detailed, finite rate chemistry. The results are validated against OH-LIF measurements. Further investigations were done with hydrogen blended in natural gas as fuel for this combustor [8]. The nature of the reaction zone was studied by OH-PLIF and

† corresponding author
Email: R.P.Sampat@tudelft.nl

chemiluminescence. It was seen that the jet velocity influenced the recirculation rate. This in turn governed the ignition delay and stabilization of the reaction zone.

Premixed FC can prove to be advantageous in terms of flame zone stabilisation thereby overcoming lean blow off limits [9], an issue seen in lean premixed gas turbine combustors. In principle, premixed FC should follow the emissions profile of a premixed turbulent flame, however, due to the practical nature of a combustor such as recirculation and heat losses may cause some differences in NO_x formation.

In this article we study emissions formation in a partially premixed FC Combustor operated under atmospheric pressure conditions. We present an experiments informed approach of modelling. Particle Image Velocimetry(PIV) was used to measure velocity vectors along a plane in the combustor and thermocouples were used to measure temperatures at discrete points in the combustor. The resultant data was used to construct a chemical reactor network model that was evaluated with and without heat-loss to provide species concentration distribution in the combustor. These results were analysed to gain insights into NO_x and CO formation in this combustor under varying operating conditions.

2 Experimental Setup

The partially premixed FC Combustor in the Clean Combustion lab at the Faculty of Aerospace Engineering, TU Delft, is a 200kW combustion system. The combustor has a burner head with 12 nozzles located at a radial distance, 65 mm from the central axis. The nozzles are configured such that the fuel nozzle is located coaxially upstream of the main nozzle as shown in the cut-section schematic in Fig 1. There are two plenums in the burner head, one for fuel and one for air which act as distribution manifolds from one source pipe to 12 nozzles. The main nozzle pipe has a length of ≈5 diameters from the air plenum, before injection into the chamber and serves as a mixing duct for fuel and air. Methane is used as fuel and air as oxidizer. CO_2 and N2 can be added to the main air flow to dilute the oxygen content in order to controllably reach Flameless Combustion inlet conditions.The combustor is a blowdown system, i.e. the source of air, fuel and other gases are pressurized tanks, followed by a series of pressure regulators and massflow controllers to specify the exact flow rate. The mass flow controllers are Bronkhorst EL-flow meters that provide a constant massflow, irrespective of the temperature and pressure of gas during operation. The facility is equipped with a 48kW electric heater to preheat the air for experiment repeatability and stable operation. The combustion chamber is either a quartz pipe or a stainless steel 304 pipe, depending on the experiments conducted. The quartz pipe is used for optical diagnostics such as PIV when sufficient optical access is required, whereas the steel chamber is used during intrusive measurements with probes such as thermocouple measurements

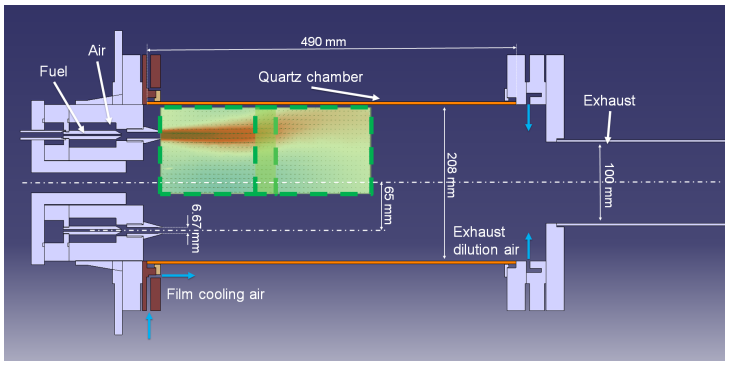

FIGURE 1: Combustor cut section schematic with PIV measurement plane. The green dashed planes indicate the overlapping fields of view of the two cameras.

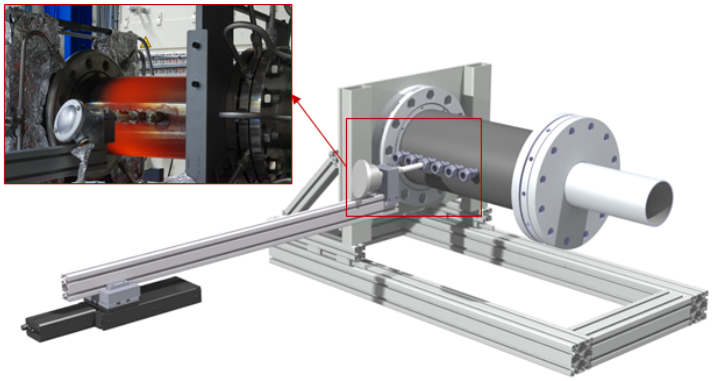

FIGURE 2: Schematic of thermocouple mounted on traverse system to measure temperature through access ports at different axial locations along the combustor.

where a physical access port is welded onto the side of the chamber, as shown in Fig 2. The hot gases are diluted by addition of cold air before the exhaust section to control the temperature for the physical integrity of the exhaust ducts and maintaining a standard exit condition for all experiments. The combustor wall is cooled by a film of air on the outside, blown through an annulus jet on the burner head as shown in the schematic in Fig 1.

The combustor was operated at 60 kW thermal power for the results shown in this article and conditions such as equivalence ratio and external nitrogen dilution are changed around this constant condition. The operating condition is monitored such that a steady burner head temperature and inlet air temperature are achieved before acquiring data. The heater is set to the same temperature for every run which ensures that the air inlet temperature is constant irrespective of the temperature of the surroundings and the external air/gas feed system.

TABLE 1: COMBUSTOR OPERATING CONDITIONS

Case	Thermal Power (kW)	Pressure (bar)	Equivalence Ratio (ϕ)	Nitrogen flow rate (lnpm)	Air Pre-heat (°C)	O_2%
1	60	1.01325	0.6	0	350	21
2	60	1.01325	0.8	0	350	21
3	60	1.01325	0.8	450	350	15.5

TABLE 2: PIV SETUP SPECIFICATIONS

Field of View Camera 1/2	130.2 /131.2 mm
Overlap between cameras	24.7 mm
Laser sheet thickness	1 mm
Acquisition frequency	15 Hz
dt case 1/2/3	3.5 /6 /3.5 μ s
Resolution of Camera 1/2	19.6/19.5 pixel/mm
Interrogation window size in final pass	24x24 pixel
Window overlap in final pass	75%
Vector spacing	305.6 μm
Number of images acquired: case 1/2/3	1800 /1750 /600

3 Measurement Technique

Experiments were performed on the Combustor to gather data on the velocity and temperature field. This is used to generate and validate a chemical reactor network which is solved for emission species. The resultant solution is further analyzed to obtain species formation rates within the combustor.

Velocity field is measured by Particle Image Velocimetry (PIV) under reacting conditions. TiO_2 particles are used as seeding material with a mean diameter of 0.5 micron. An Evergreen double pulse laser with 200 mJ peak pulse energy at 532 nm is used to illuminate the particles in a plane. An average sheet width of 1 mm was maintained throughout the field of view. Two LaVision Imager sCMOS cameras with Micro Nikkor 105 mm lenses with f# 11 were used in 2D2C mode to capture an extended field of view with sufficient magnification. The field of view of the first camera, located nearer to the burner head, was 130.2 mm and that of the second camera was 131.2 mm in the direction along the combustor axis. The overlap between the frames was 24.7 mm. A polarization filter was placed in front of the lens of each camera to reduce reflections from surfaces and a 532 nm bandgap filter was used to eliminate background noise and flame luminescence.

During reacting flow PIV, the main challenge was that the TiO_2 particles carried by the external recirculation zone, pit against the hot walls and stuck to it, degrading the transparency and hence the ability to visualize the particles. It was seen that the tube stayed transparent enough for around 30 seconds with seeding after which the contrast in the regions near the wall degraded severely. An extension to 60-90 seconds was possible to visualize regions away from the wall, while foregoing the external recirculation information. External film cooling of the combustor seemed to prolong the life of the pipe by reducing sites of permanent fusion of particles on the quartz wall. The fuel stream was seeded by bypassing a portion of the flow through a seeder and then combining it with the remaining flow. This was then injected through the single nozzle that was imaged.

The seeder consists of a turbulent jet flow that impinges onto a bed of seeding powder. The exit is on the same side as the inlet such that the flow changes direction and recirculates in the vessel. Larger particles are either ejected by centrifugal forces produced in this recirculation or broken up in a throttle valve placed at the exit of the vessel that produces high strain rate in the flow.

Temperature measurements were performed using a steel combustion chamber with discrete ports on the side of the wall, as shown in Fig 2. The inset shows a photograph of the setup during operation and the cherry red color or hottest zone puts an estimate of the wall temperature in the range of 700-800 °C. A ceramic sheathed, S-type thermocouple is inserted through the ports and is traversed radially using a Zaber, automatic linear traverse system. This allows repeatable traverse at predetermined radial locations. The ports are sealed with a layer of ceramic rope gasket in a ferrule fitting, instead of the steel ferrule. The nut is adjusted such that the gasket is tight enough to prevent gas leakage but loose enough to allow for traversal of the thermocouple. All thermocouple data is acquired through an NI9213 module mounted on a NI-cRIO embedded industrial controller. The module has inbuilt cold-junction temperature compensation. The thermocouple is a cylinder with a diameter of 15 mm. The distance of the hot junction from the outer tip of the sheath is 13 mm, hence it is assumed that the measurements are averaged over a radius of 6.5 mm centred at a point 6.5 mm away from the tip along the thermocouple stem.

There are 6 ports through which a probe may be inserted through the steel combustor as shown in Fig 2. In this paper, we present measurements at Port 3 and Port 5. Port 3 and 5 are at an axial distance of 140 mm and 240 mm respectively from the burner head. The measurements are corrected to account for radiation loss from the probe, radiation influx from the combustor wall, radiation from the hot gas surrounding the probe and

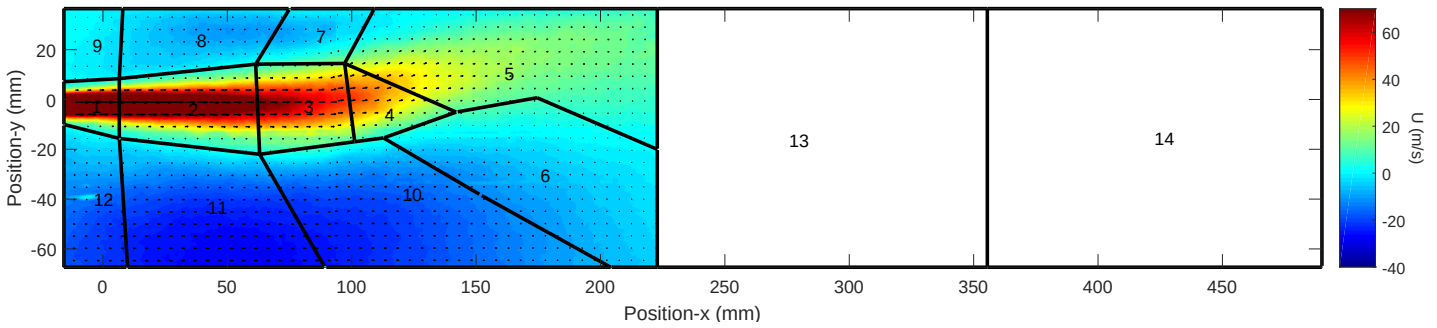

FIGURE 3: CRN drawn over axial velocity contour plot for 60kW, $\phi = 0.8$

convective heat transfer from the flow, according to Eqn 1.

$$h_{c,g}T_g + \epsilon_c(\sigma\epsilon_g T_g^4 + \sigma\epsilon_w T_w^4) = \sigma\epsilon_c T_c^4 \tag{1}$$

, where ϵ_g is the emissivity of the gas in the vicinity of the probe location, ϵ_w is the emissivity of the combustor wall, ϵ_c is the emissivity of the thermocouple, T_g is the temperature of the gas in the vicinity of the probe, T_w is the combustor wall temperature and T_c is the temperature measured by the thermocouple. Equation 1 is solved for T_g, except for at radial location coinciding with the wall. In that case convection is assumed to be zero because of no slip condition at the wall ($h_{c,g}$=0), radiation effect of gas is ignored, reducing the equation to Eqn 2, which is solved for the wall temperature (T_w).

$$\epsilon_c\sigma\epsilon_w T_w^4 = \sigma\epsilon_c T_c^4 \tag{2}$$

Velocity data is used to obtain the local velocity at the measurement point and estimate a heat transfer coefficient, $h_{c,g}$, based on the Nusselt number from correlation in Eqn 3 [10].

$$Nu_D = 0.3 + \frac{0.62Re_D^{1/2}Pr^{1/3}}{\left[1+(\frac{0.4}{Pr})^{2/3}\right]^{1/4}} \tag{3}$$

4 Chemical Reactor Network Modelling

The combustor is modelled as a Chemical Reactor Network (CRN), a network of zero dimensional perfectly stirred reactors.The CRN was generated through a semi-automated process. The reactors were manually demarcated by specifying the spatial coordinates of nodes surrounding a reactor. In this case, the velocity field from PIV and the nature of the recirculation zones is used as a basis. A Matlab code was written to accept coordinates of nodes, a map of edges defined by the node connectivity and the nodes arranged in clockwise direction for each reactor. The code goes on to draw edges in space, calculate the reactor area and velocity flux associated with each edge. The resultant CRN can be seen in Fig 3, which is for Case 2. Similar CRNs from average velocity fields of the other two cases were generated and solved.

Velocity flux calculation is crucial as this is where the measured PIV data is used to "inform" the CRN model. A line is drawn between two defined nodes. The line is populated with points with a separation, d_{node}, equal to the distance between two vectors in the PIV image. Next, a search operation is done for valid vectors, around a single point, in a radius equal to $d_{node}/2$ in the PIV mesh. If no valid vectors are found, the search radius is doubled and the process is repeated till a valid vector is found. The velocity vector associated with that point is the average of the vectors that are found. A unit vector perpendicular to the line is calculated as

$$\hat{n} = \frac{1}{\sqrt{(1+1/m^2)}}\hat{i} + \frac{(-1/m)}{\sqrt{(1+1/m^2)}}\hat{j} \tag{4}$$

, where m is the slope of the line. Velocity flux through a line is the sum of the products of the differential area and dot product of velocity vector and unit vector perpendicular to line over the points on the line.

Reactor areas are calculated by integrating over the cell area from the PIV image based on the associated node coordinates. The PIV plane is treated as a periodic section such that a volume is obtained by revolving the aforementioned area by an angle of 30°, with a radius equal to the radial distance between the reactor geometrical center and the central axis of the combustor. The reactors associated with the jet (1,2,3,4) are treated differently, by simply multiplying the area from PIV grid by the nozzle diameter(6.67mm).

The above information is fed to a Python code that further processes it into a CRN model based in Cantera [11]. The velocity flux at edges is used to define the ratio in which massflow going

out of a reactor is split between its neighboring reactors. The assumption here is that the ratio is only dependent on the product of velocity and area, not on density, which is true for a CRN model as a single perfectly stirred reactor is homogeneous and the thermodynamic state of the gas stream exiting it is the same irrespective of the stream's connection. A mass balance matrix equation is set up as shown in Eqn 5, where the values of α_{ij} are obtained from velocity flux ratios mentioned earlier.

$$M_k - \sum_{j \neq k}^{N} \alpha_{kj} M_j = \sum f_k \tag{5}$$

where M_k is the total outflow from k^{th} reactor, M_j is the total outflow from j^{th} reactor, α is the fraction of outflow from j^{th} reactor flowing into k^{th} reactor and f_k is any other source of mass inflow. As can be seen, all mass flows, M, are defined as an outflow from a reactor. This results in a $AX = B$ type system where A is a NxN matrix and B is a vector of source terms. In the current code, B contains the inflow boundary mass flow values. The solution to the system is found giving the total outflows as a result. The coefficients from the matrix A are used to assign the correct fractions of the total exit massflow from a reactor to its neighbours. Thus, the flow connectivity between reactors and reactor volumes is obtained from PIV data and the inlet massflow is known from the value set by the massflow controllers. The resultant CRN is solved as a reactor network system in Cantera.

Chemical Reactor Networks were individually generated and solved for each case. GRI-Mech 3.0 chemical mechanism was used to model detailed finite rate chemistry. Figure 3 shows a 14 reactor CRN overlaid on axial velocity contour plot. The reactors were generated by the methodology stated above, while reactors 13 and 14 were placed to represent the latter part of the combustor that was not imaged in the PIV measurements. The additional length of the combustor would provide extra residence time for evolution of NO_x and CO, hence making it necessary to include it in the model. This section contains a transition region from expanded jet and a plug flow region downstream, which is why it is modelled with two reactors in series. Based on the operating condition, Table 1, the inlet gas state and massflow is specified. This serves as the inlet boundary condition for which the CRN is solved. The solution allows extraction of reactor gas state for each reactor.

4.1 Heat Loss model

All cases of operation were also simulated in the CRN model with heat loss. Heat loss is modelled via a wall object associated with a reactor. A heat flux and wall area are defined that is used as a heat sink in the evaluation of the energy equation of the reactor network. Heat loss is calculated from the following formula,

$$Q_{loss} = \sigma \varepsilon_{wall} T_{wall}^4 - \sigma \varepsilon_{wall} \varepsilon_{surr} T_{surr}^4 + h(T_{wall} - T_{film}) \tag{6}$$

Convective heat transfer coefficient of film cooling, h, is obtained from thermocouple measurements done on the external surface of the combustor to estimate the Nusselt number. An average value obtained over the length of the combustor is used for this calculation. T_{wall} is obtained by interpolating between them thermocouple measurements done in the combustor, on the burner head and the exhaust duct, based on the wall axial location.

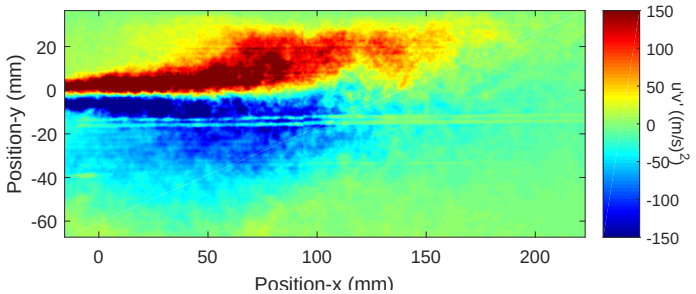

FIGURE 4: Reynolds Shear stress distribution for 60kW, $\phi = 0.8$

5 Results

5.1 Velocity field

The PIV measurements result in two component vectors over a plane. The images from two cameras are stitched together to obtain an extended field of view at higher resolution than would have been by imaging the entire field of view with one camera. Contour plot of axial velocity is seen in Fig 3 with vectors overlaid. On the y-axis, the nozzle center is located at y=0mm, the combustor centerline is at the lower x-axis of the frame and the combustor wall is towards the upper edge of the frame. The wall is not imaged in the result as only spurious data was obtained a few millimetres from the wall due to the pipe curvature and reflections. One can observe two recirculation zones, one central recirculation zone (CRZ) from the jet towards the combustor axis and another peripheral recirculation zone (PRZ) from the jet towards the combustor wall. The PRZ forms upstream of the CRZ. The central jet also shows a bend towards the wall starting from x≈100 mm. This is characteristic of a jet near a wall, where the Coanda effect driven by suction due to high velocity flow near a wall, makes the predominant flow attached to the wall.

The flow is turbulent and subject to high shear stress due to the main jet and recirculation being in the opposite directions. Figure 4 depicts a distribution of Reynolds shear stress. A high magnitude is seen at the interface of the jet and its surroundings. High positive value is seen where the jet attaches to the wall and in the section of the flow that changes direction to recirculate in

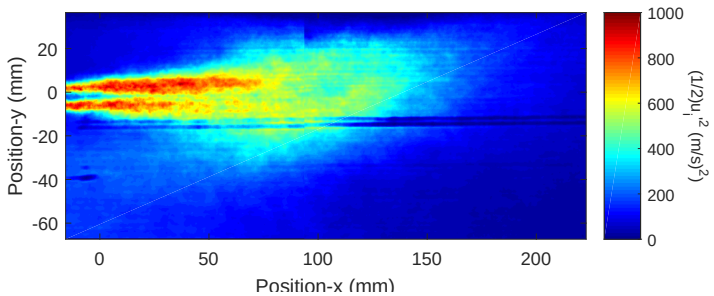

FIGURE 5: Turbulence Kinetic Energy distribution for 60kW, $\phi = 0.8$

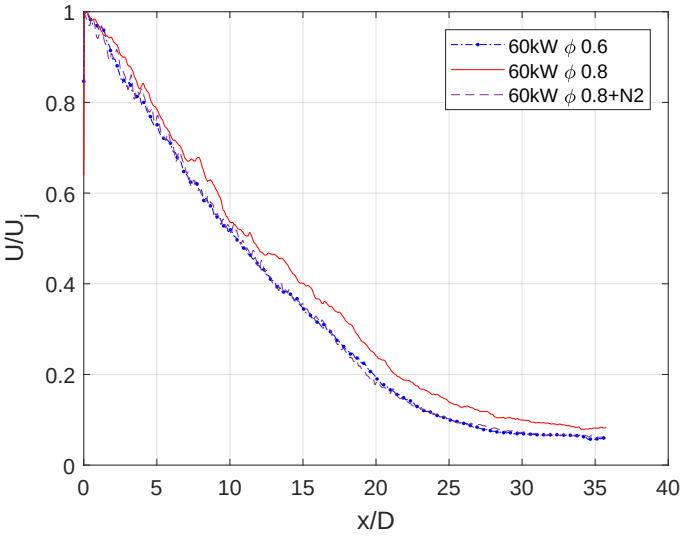

FIGURE 6: Axial velocity vs x/D

the Peripheral Recirculation Zone. This is not as prominent at the turning point of the central recirculation zone, however, higher shear stress is seen in region where the CRZ meets the jet in the jet near-intermediate field, showing a distributed region of shear stress. The PRZ does not have this kind of a distributed region of shear stress.

The turbulent kinetic energy distribution in Fig 5, shows high energy in the shear region and a degrading plume tilting towards the combustor wall, further downstream. The PRZ and CRZ have a low turbulent kinetic energy content, possibly due to destruction of fluctuations due to jet expansion and heat addition. There are horizontal streaks of anomalous data in Fig 4 and Fig 5 at y≈-19 mm. These arise due to internal reflections of the laser sheet from the quartz pipe and the burner head surface. These are spurious data points and not meant to be considered for analysis.

Further information of the flow is obtained by plotting line plots along the jet centerline. The jet centerline is tracked by finding the radial location with the highest axial velocity for a line perpendicular to the combustor centerline at a given axial

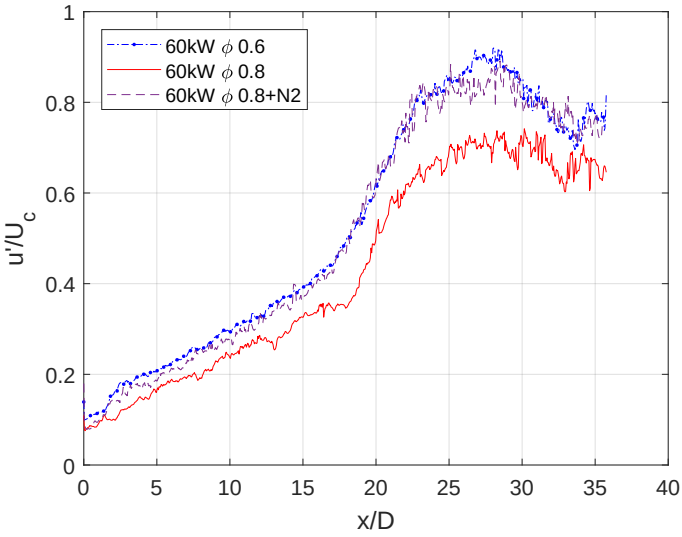

FIGURE 7: Turbulence intensity v/s x/D

location. From Fig 3, it is estimated that the jet centerline curves away from the combustor centerline at x≈75 mm. Figure 6 shows a linear decay in normalised axial velocity along the jet centerline up till x/D=18 beyond which there is decrease in decay rate till the curve flattens at x/D=30. The transition point corresponds to the location where the jet turns towards the wall and attaches to it. This trend is similar for all three operating conditions.

A comparison of turbulence intensity in Fig 7 between the three different operation conditions shows that they have similar characteristics till x/D=25. There are two linear trends, x/D=0-17 and x/D=18-25, with two different slopes. The first trend line corresponds to the jet emanating from the nozzle, which shows an increasing turbulence intensity. The second line corresponds to the wall attachment region and shows a higher rate of increase of turbulence intensity. Beyond x/D=25, the cases with ϕ=0.6 and ϕ=0.8+N_2 have a higher turbulence than that of ϕ=0.8. The higher temperatures of a richer equivalence ratio may lead to higher viscosities of gases formed during combustion leading to a dissipation of fluctuations.

5.2 Temperature measurements

Temperatures were measured at five radial locations for Port 3 and 5, each. Measurements of Port 3 are shown in Fig 8. Case 1 and 3 have similar temperature values, while Case 2 has a higher temperature. Port 3 (axial distance=140 mm from burner head) corresponds to the axial location where the jet impinges on the combustor wall. The region towards the centerline seems to have a higher temperature and a steep drop is seen near the wall, due to heat loss effects.

Port 5 (axial distance=240 mm from burner head) is where the flow becomes more plug like. Figure 9 shows the temperature

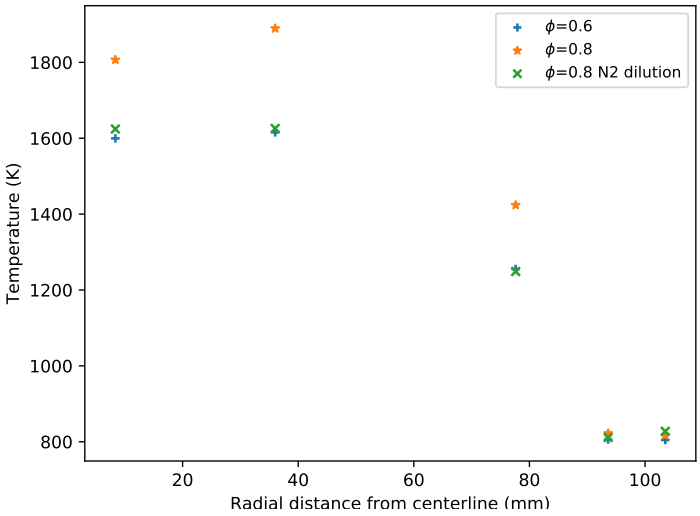

FIGURE 8: Temperature measured at Port 3.

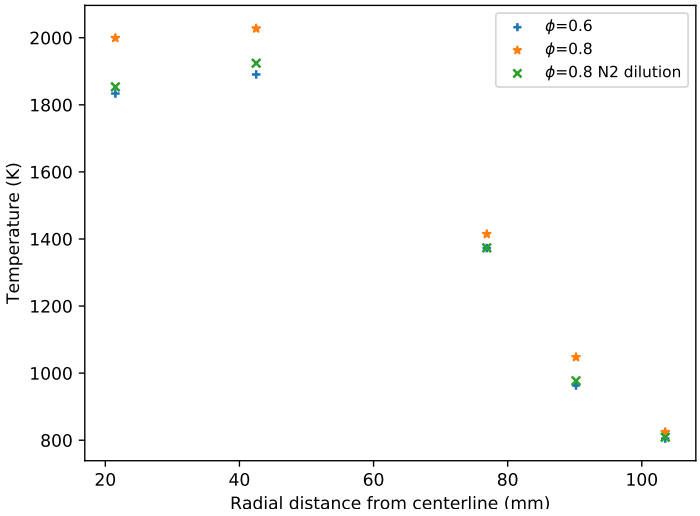

FIGURE 9: Temperature measured at Port 5.

distribution at Port 5 and here too, Case 2 has higher temperatures. However, there seems to be a larger temperature gradient at the wall than at Port 3. The wall temperatures are measured to be 800 K after correction, which is an under prediction based on the colour of the hot chamber that was observed during experiments. The chamber varied from dark red to cherry red giving an estimate of 900-1100 K.

5.3 Temperature and Species concentrations from CRN

The state of each reactor of the CRN is analysed here in terms of temperatures and species concentrations. Reactors 1-4 are in series representing the jet. Reactor 5 represents the region where the jet curves to attach to the wall and reactor 6 is the parallel flow that turns towards the center to form the CRZ. Reactors 7-12 form the CRZ and PRZ, of which reactors 7-9 are in the PRZ and are in contact with the outer wall. The temperatures are plotted in Fig 10. Temperature rises from reactor 1 to 5 indicating heat release in these reactors. In adiabatic operation cases, it remains almost constant in the remaining reactors. In cases with heat loss, there is an evident drop in reactors 7-9, which form the PRZ region. This is also where the flow comes in contact with the combustor wall, where it loses heat to the surroundings.The case with N_2 dilution has a significantly lower temperature in the PRZ (8 and 9) which may also be an extinction event. The combustor exit temperature can be seen in reactor 14 and the cases with heat loss do show a lower temperature than their adiabatic counterparts. Overall, it seems that Case 2 and its heat loss counterpart have the highest temperatures followed by adiabatic Case1 and 3. Case 1 and 3 with heat loss show the lowest reactor temperatures.

The effect of varying temperature along the combustor and heat loss can be seen in minor species distributions. Figure 11 shows NO_x distribution across all reactors for the three operation cases along with their heat loss counterparts. NO_x is seen to rise from reactor 1-6, which is consistent with increasing temperatures. For adiabatic cases, there is a rise in NO_x in reactors 7-9 (PRZ), probably due to the extended residence time that favours NO_x formation at high temperatures. The NO_x levels remain more or less constant in the CRZ and reactors 13-14 (second half of combustor). However, in Case 2, NO_x increases in the last reactor. Comparing the adiabatic and non-adiabatic cases reveals a lower NO_x level in cases with heat loss. In case of heat loss, lower NO_x is seen in reactors 7-9 (PRZ) compared to the adiabatic cases. Case 1 with heat loss and Case 3 with heat loss, have similar NO_x levels and the lowest out of all the cases. Highest NO_x levels are seen in Case 2 followed by Case 2 with heat loss.

CO distribution is shown in Fig 12. For Case 1 and 3 (with and without heat loss), CO starts at a low level in reactor 1 and then increases in reactor 2 beyond which it decreases up till reactor 6. This may indicate slow breakdown of methane into intermediate species initially along the jet. Reactor 7-9 and 10-12 show decreasing CO levels compared to reactor 4 (from where the recirculation originates) but with different magnitudes. The extended residence time of recirculation enhances CO consumption leading to a lower concentration in those regions. Similarly, in the exhaust rectors, 13 and 14, a decrease in CO level is seen compared to 5 and 6. In Case 2, CO starts off high in reactor 1 and decreases in subsequent reactors till it reaches a constant value beyond reactor 6. Case 2 with heat loss shows deviation in reactor 5-14. It shows lower CO levels than the adiabatic counterpart (which has higher temperatures). Higher temperatures lead to CO_2 dissociation, hence pushing the equilibrium in the reverse direction, leading to higher CO concentration. Heat loss in the PRZ (reactor 7-9) reduces the dissociation, leading to reducing CO levels and higher CO_2. This recirculates and causes

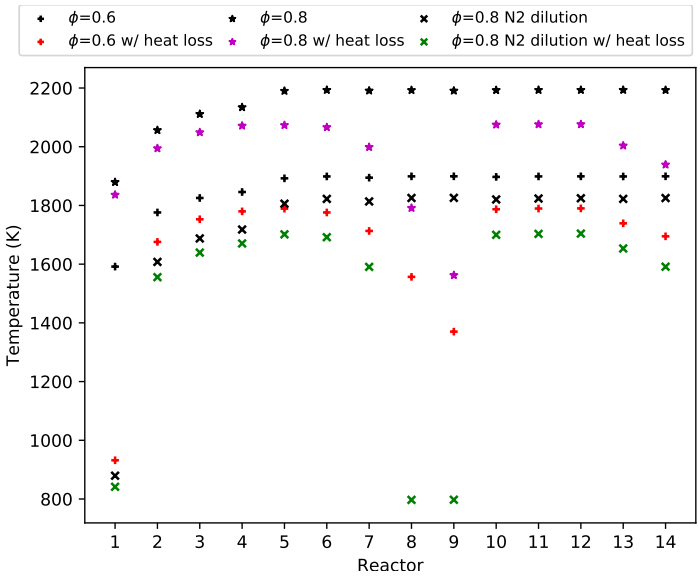

FIGURE 10: Temperature distribution across reactors for different operating conditions

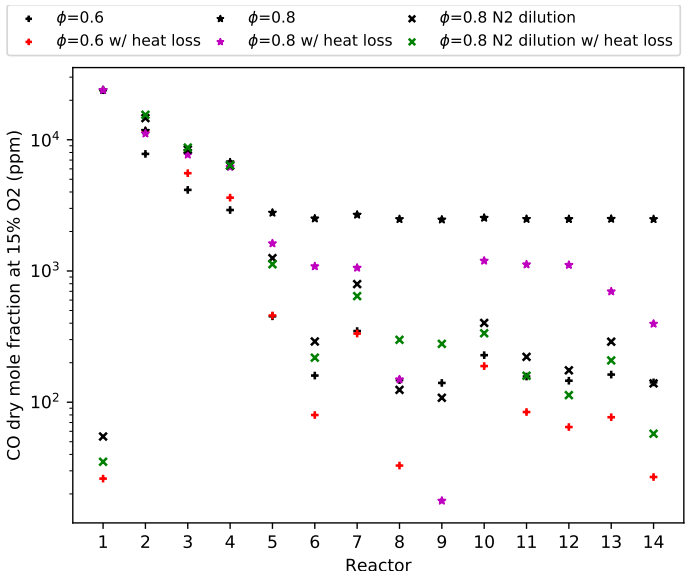

FIGURE 12: CO distribution across reactors for different operating conditions

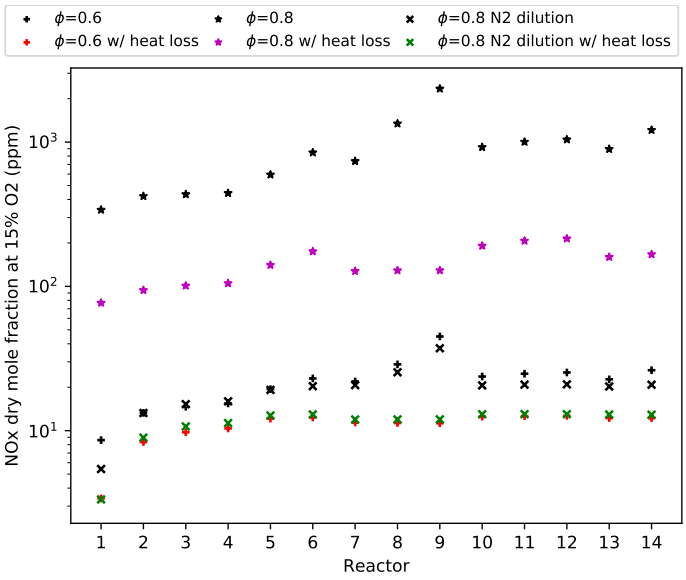

FIGURE 11: NO_x distribution across reactors for different operating conditions

a positive feedback loop by mixing with the fresh reactant jet. This is seen in the CRZ (reactor 10-12) also having reduced CO levels compared to Case 2 without heat loss but maintains almost a constant value in this region. A similar reasoning also works for the observation of lower CO levels in Case 1 with heat loss compared to adiabatic version of Case 1. Case 3 on the other hand, shows higher CO levels in reactor 8 and 9 (PRZ) in case of heat loss compared to adiabatic version. The temperatures in this case also drop below 1000 K, thus the CO oxidation reaction becomes way slower, leading to higher CO levels here.

The oxygen concentration in the reactors as seen in Fig 13, gives an indication of the level of dilution in different regions. Case 1 stabilises at 8% O_2 while Case 2 and 3 go below 4%. It is important to note that the recirculation regions, reactors 7-12, have a low O_2 percentage and this composition recirculates back into the fresh reactants in reactors 1-4.

6 Conclusion

Operation characteristics of Flameless Combustor were studied experimentally by measuring velocity fields (PIV) and temperature (thermocouples). We identify central and peripheral recirculation zones, jet impingement on the combustor wall and a transition from a jet to a wall attached flow. Region of high shear stress and turbulence kinetic energy are observed in the shear region of the jet with the recirculation. High Reynolds shear stress is seen to extend till the flow turns to form the PRZ, while on the CRZ side, a broadening of high stress regions is seen in the region where the recirculated flow meets the fresh reactant jet. A distinction between the 3 cases is seen in the turbulence intensity along the centerline, where Case 2 shows a higher decay beyond x/D=25, possibly due to higher temperatures in the region leading to higher viscosities.

A CRN is generated based on the velocity field measurements for each case. This is supplemented by a heat loss model based on the wall temperature measurements. The CRN is solved

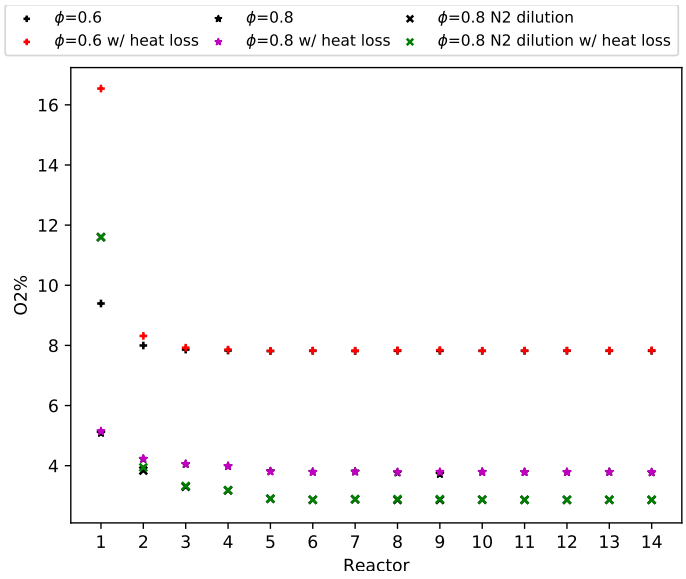

FIGURE 13: O_2 distribution across reactors for different operating conditions

to obtain temperature and species distribution in the Combustor. NO_x levels are seen to be lower for Case 1 and 3, for both adiabatic and heat loss conditions, than Case 2. This is because of low temperatures and low O_2 concentration in Case 3 (with N_2 dilution). NO_x in the recirculation zone and CO formation are seen to be sensitive to heat loss modelling. The dissociation of CO_2 into CO and O_2 plays a role in determining the CO concentration and results in lower CO in lower temperature regions. However, in Case 3 with heat loss, the temperature in the PRZ drops significantly below 1000K which results in higher CO levels than its adiabatic counterpart as CO is not oxidised to O_2. Finally, O_2 mole fractions reveal that the recirculation zones are responsible for mixing low O_2 concentration gas with fresh reactants, thereby creating conditions conducive for Flameless Combustion.

The reaction zone is sustained by the recirculation of high temperature products in this combustor. This is motivated by the presence of product gases having high temperature along with high CO and low O_2 levels in the jet region where recirculated products are mixing. The data also shows that the combustor can be operated stably under lean premixed conditions and emissions lowered by increasing excess air and dilution. The experiments informed CRN helps predict NO_x and CO formation in different regions of the combustor and may serve as a testing model for different operation conditions such as variation in load, external cooling and dilution. Further experiments shall be performed to measure gas composition in the combustor to validate the CRN results.

ACKNOWLEDGMENT

The authors would like to thank Jos van Meurs for his hard work on the fabrication and assembly of various components of the combustion rig.

REFERENCES

[1] Wünning, J., 1997. "Flameless oxidation to reduce thermal no-formation". *Progress in Energy and Combustion Science,* ***23***(1), pp. 81–94.

[2] Cavaliere, A., and de Joannon, M., 2004. "Mild Combustion". *Progress in Energy and Combustion Science,* ***30***(4), jan, pp. 329–366.

[3] Sorrentino, G., Cavaliere, A., Sabia, P., and Ragucci, R., 2020. "Diffusion Ignition Processes in MILD Combustion : A Mini-Review". pp. 1–8.

[4] Perpignan, A. A., Gangoli Rao, A., and Roekaerts, D. J., 2018. "Flameless combustion and its potential towards gas turbines". *Progress in Energy and Combustion Science,* ***69***, nov, pp. 28–62.

[5] Vaz, D. C., Van Buijtenen, J. P., Borges, A. R. J., and Spliethoff, H., 2004. "On the stability range of a cylindrical combustor for operation in the flox regime". *ASME Turbo Expo 2004: Power for Land, Sea and Air,* ***June***, pp. 511–516.

[6] Luckerath, R., Meier, W., and Aigner, M., 2008. "FLOX[®] Combustion at High Pressure With Different Fuel Compositions". *Journal of Engineering for Gas Turbines and Power,* ***130***(1), p. 011505.

[7] Schutz, H., Luckerath, R., Kretschmer, T., Noll, B., and Aigner, M., 2008. "Analysis of the Pollutant Formation in the FLOX® Combustion". *Journal of Engineering for Gas Turbines and Power,* ***130***(1), p. 011503.

[8] Sadanandan, R., Lückerath, R., Meier, W., and Wahl, C., 2011. "Flame Characteristics and Emissions in Flameless Combustion Under Gas Turbine Relevant Conditions". *Journal of Propulsion and Power,* ***27***(5), pp. 970–980.

[9] Özdemir, I. B., and Peters, N., 2001. "Characteristics of the reaction zone in a combustor operating at mild combustion". *Experiments in Fluids,* ***30***(6), pp. 683–695.

[10] Churchill, S. W., and Bernstein, M., 1977. "A Correlating Equation for Forced Convection From Gases and Liquids to a Circular Cylinder in Crossflow". *Journal of Heat Transfer,* ***99***(2), may, pp. 300–306.

[11] Goodwin, D. G., Speth, R. L., Moffat, H. K., and Weber, B. W., 2021. Cantera: An Object-oriented Software Toolkit for Chemical Kinetics, Thermodynamics, and Transport Processes.